RSC Advances

PAPER

View Article Online
View Journal | View Issue

Cite this: *RSC Adv.*, 2021, **11**, 22365

Synthesis of ZSM-5 zeolites from biomass power plant ash for removal of ionic dyes from aqueous solution: equilibrium isotherm, kinetic and thermodynamic analysis†

Guangbing Liang,[a] Yanhong Li,*[a] Chun Yang,[b] Xun Hu,[c] Qingyin Li[c] and Wenbo Zhao[a]

In this work, industrial biomass power plant ash was used to synthesize the ZSM-5 zeolites for the first time with the original intention to turn value-added material into wealth, and then committed to adsorption performance testing. Typical chemical structure and morphology of ZSM-5 zeolite were identified by comprehensive technologies. Uniquely, it was found that there was a low pressure hysteresis loop which was caused by crossed 10-membered rings in the N_2 adsorption–desorption isotherm. To investigate the adsorption performance for dyes, the zeolite samples were used to remove cationic (MB) and anionic (CR) dyes from aqueous. The results demonstrated that when it came to adsorbing MB, the isotherm was in line with the Redlich–Peterson model (R^2 > 0.99), whereas it was matched up with the Sips model (R^2 > 0.99) for adsorbing CR. Kinetic models were assigned to the pseudo-second order equation ($R^2 \geq 0.99$) along with remarkable intraparticle diffusion. In the end, thermodynamic parameters were $\Delta G^0 < 0$, and $E_a > 0$. Especially, adsorbing MB was $\Delta S^0 > 0$, and $\Delta H^0 > 0$, whilst adsorbing CR was $\Delta S^0 < 0$, and $\Delta H^0 < 0$, which indicates that electrostatic interaction plays a significant role in the whole process. All in all, this work might encourage novel attempts to dispose of industrial biomass ash.

Received 17th May 2021
Accepted 18th June 2021

DOI: 10.1039/d1ra03847h

rsc.li/rsc-advances

1 Introduction

Greenhouse gas (GHG), generated from the consumption of fossil fuels, has caused intractable environmental issues along with the rapid development of urbanization and industrialization. To fulfill its emission reduction target, China has promoted the usage of renewable clean energy intensively, and announced that the proportion of non-fossil energy consumption will rise to 20% for primary energy in 2030.[1] Therefore, biomass resources, such as agricultural residues, forestry residues, and municipal solid wastes are alternatives to the dependency on conventional energy, in particular coal.[2] Growing quantities of biomass resources will reach 1.4 billion tons of Standard Coal Equivalent (TCEs) in China by 2050, and more than 60% will be usable for energy production with approximately 10% CO_2 emission reduction.[3,4] Indeed, power generation is still the most common mode of biomass industrial utilization currently in China, whilst biomass power plants initially appeared in 2004 which account for 1% total electricity production.[5,6] Undoubtedly, the Chinese government will facilitate the development of biomass electricity generation. At the same time, it has been revealed that 95–97% biomass is directly combusted to generate energy in power plants, whereas the ash yield can be up to 6–7% on average.[7,8] Therefore, large amounts of power plant ash will be landfill, accounting for around 70% of total ash quantity,[9] while ash landfill could bring out some environmental issues as well, *e.g.* groundwater eutrophication (nitrogenous and phosphorous matters),[10] heavy metal contaminated soil,[4] *etc.* Consequently, it is essential to seek a reasonable solution for turning this solid waste ash into wealth.

On the other hand, the World Bank elucidated that annually 100 tons of textile dyes would be released into water bodies, which account for 17–20% of industrial water pollution.[11] Colored effluents not only can damage to the aquatic ecosystems *via* inhibition of photosynthesis due to their non-biodegradable, but also will threaten public health,[12] *i.e.* anorexia, anemia, cancer, *etc.* Inevitably, the treatment operations of effluents have been carried out. In contrast with the electrochemical process,[13] ultrafiltration,[14] ultrasound irradiation,[15] liquid–liquid,[16] and biological treatment,[17] adsorption is

[a]Faculty of Chemical Engineering, Kunming University of Science and Technology, Kunming, 650500, China. E-mail: liyh_2004@163.com
[b]College of Chemical Engineering and Environment, China University of Petroleum, Beijing, 102249, China
[c]School of Material Science and Engineering, University of Jinan, Jinan, 250022, China

† Electronic supplementary information (ESI) available. See DOI: 10.1039/d1ra03847h

flexibility, effectiveness, insensitivity, cheapness, and selectivity process.[18] Generally speaking, the types of adsorbents are extensive,[19] and zeolites are always attractive, reliance on the advantage of high surface area, large pore volume, and better thermal stable.[12] Shaban *et al.*[20] reported that the maximum adsorption capacity of Na–P zeolite composite for methylene blue (MB) was 46.29 mg g^{-1}. Oukil *et al.*[21] found that Ni/Co USY zeolite composite could adsorb MB up to 59.88 mg g^{-1}. On the contrary, ZSM-5 zeolite composite's maximum adsorption capacity of MB was 81.90 mg g^{-1}, clarified by Sabarish and Unnikrishnan.[22] It was proved that ZSM-5 zeolite has a significant potential for removal of dyes, by virtue of unique pore structure and excellent shape selectivity.

Prior to this work, coal fly ash or various clays were commonly used to synthesize ZSM-5 zeolite,[23–26] whilst substantially the commercial aluminum (Al) sources have to be extra added. Subsequently, rice husk burned ash was alternative to be silicon (Si) sources, but no further changes.[27] In this study, two ashes obtained from biomass power plant and laboratory, respectively were novel to synthesize ZSM-5 zeolite *via* a green and economical route without any commercial Si or Al additive for the first time. To fulfill the aim of waste controlled by waste, the simulated testing of adsorption performance on two typical textile dyes (methylene blue, MB & Congo red, CR) was given out by sample zeolite. Basic on the adsorption process of the interaction between adsorbate and adsorbent, equilibrium isotherms, kinetic equations, and thermodynamic parameters were evaluated. The impetus of this work was anticipated that this strategy would play a vital role in biomass power plant ash treatment for further study, or pave a facile way for resource utilization of waste biomass ash.

2 Experimental section

2.1 Materials and reagents

The first ash (A-1) was used as essential nature Si/Al sources, which was collected from power plant located in Jiangsu province, whose feedstock contained rice straw and husk blend of wood chips. The second ash (A-2) was used as complementary nature Si source, which was combusted with laboratory furnace, whose feedstock was only rice husk collected from Sichuan province. Both ashes were obtained in autumn, and the chemical compositions of A-1 and A-2 were list in Table S1.† Sodium hydroxide (NaOH, CAS: 1310-73-2) was analytical grade purchased from the Sinopharm Chemical Reagent Co., Ltd. Tetrapropylammonium hydroxide (TPAOH, CAS: 4499-86-9), methylene blue (MB, CAS: 7220-79-3) and Congo red (CR, CAS: 573-58-0) were purchased from the Aladdin Biochemical Technology Co., Ltd. Deionized water (pH 6.8) was used during all synthesis and treatment processes.

2.2 Synthesis of ZSM-5 zeolites

Hydrothermal synthesis of ZSM-5 zeolites is a facile and mature method, whereas the time for crystal growth is always too long,[28,29] generally several days or even more than 10 days. In this case, a simple step was added to shorten the reaction time effectively. Precursor solution was prepared from 200 mL 0.25 M NaOH solution combined with 1.0000 ± 0.0005 g A-1 and 8.0000 ± 0.0005 g A-2 whose SiO_2/Al_2O_3 molar ratio is 100 theoretically, and stirred continuously for 4 h under ambient temperature. Then, the mother liquid was separated by filtration. Crucially, the filtrate was needed to be put statically and to stay overnight for colloidization, instead of directly going on crystal process. At this period, weak acid radical of SiO_3^{2-} and AlO_2^- would happen to hydrolyze to form sol molecular in line with following reactions. In contrast, the contact surface and reactive site of sol molecular are far more than solute molecular. Subsequently, 0.5 g TPAOH was added into colloidal sol which was loaded in a stainless steel autoclave lined with PTFE. After diverse hydrothermal synthesis conditions, the obtained zeolite was centrifuged at 9000 rpm, and dried at 100 °C for 8 h. Finally, all the samples were calcined in air at 550 °C for 5 h to remove the remained organic template. The results for synthesized ZSM-5 zeolite under diverse conditions were listed in Table S2.†

$$NaOH + SiO_{2(s)} \rightarrow Na_2SiO_3$$

$$+H_2O \xrightarrow{\text{Hydrolyzation}} H_2SiO_{3(sol)} \rightleftharpoons SiO_{2(sol)} + H_2O \quad (1)$$

$$NaOH + Al_2O_{3(s)} \rightarrow NaAlO_2$$

$$+H_2O \xrightarrow{\text{Hydrolyzation}} Al(OH)_{3(sol)} \rightleftharpoons Al_2O_{3(sol)} + H_2O \quad (2)$$

2.3 Adsorption batch testing

Synthesized ZSM-5 zeolite sample was used as adsorbent for removal of MB (cationic dyes) and CR (anionic dye) from aqueous solution. For each experiment, 0.1 g zeolite was added into 100 mL dye effluent (~pH 6.8) with diverse concentrations (25–500 mg L^{-1}) at diverse temperatures (25–65 °C) for diverse contact times (10–240 min). After shaking and centrifugation process, the remained concentrations of the effluent were tested by UV-vis spectrophotometer (MAPADA UV-1800, China) at the maximum absorption wavelength (λ_{max}) of 664 nm (MB) and 498 nm (CR), and calculated from well-established standard curve. Furthermore, the Langmuir, Freundlich, Temkin, Sips and Redlich–Peterson (R–P) isothermal models were used to investigate the adsorption mechanism. The adsorption kinetics was determined by pseudo-first-order, pseudo-second-order and intraparticle diffusion models. In terms of the van't Hoff and the Arrhenius equations, the thermodynamic parameters of the standard Gibbs free energy (ΔG^0), enthalpy (ΔH^0), entropy (ΔS^0) and activation energy (E_a) were revealed. The adsorption quantity (q), removal efficiency (%R) and adsorption efficiency (AE) for regeneration of adsorbent were calculated by corresponding equations which were all listed in ESI.†

2.4 Characterization

X-ray fluorescence spectrometer (XRF, Bruker S8 TIGER, USA) was used to determine the chemical compositions of power

plant ashes. The crystal and chemical structure analysis of synthesized ZSM-5 zeolite were tested by X-ray diffraction (XRD, Bruker AXS D8, USA), Fourier transform infrared spectroscopy (FTIR, Bruker ALPHA, USA) and $^{29}Si/^{27}Al$ magic angle spinning nuclear magnetic resonance ($^{29}Si/^{27}Al$ MAS NMR, Bruker AVANCE III 600, USA), respectively. Herein, XRD was operated with Cu Kα radiation source (λ = 1.54 Å) with 0.020° step interval and 2 s per step counter time range from 5 to 65°. FTIR spectra were working from 400 to 4000 cm^{-1} with a resolution of 4 cm^{-1}, and ^{29}Si MAS NMR spectra with high-power proton decoupling were recorded with a spinning rate of 10 kHz, a $\pi/4$ pulse length of 2.6 μs, and a recycle delay of 100 s. ^{27}Al MAS NMR spectra were recorded using a small-flip angle technique with a pulse length of 0.5 μs ($<\pi/12$) and a 1 s recycle delay and a spinning rate of 14 kHz. The chemical shifts of $^{29}Si/^{27}Al$ MAS NMR were referenced to 1 mol L^{-1} aqueous TMS and $Al(NO_3)_3$, respectively. The thermal analysis of zeolite powders and contaminated zeolite adsorbents were analyzed using thermogravimetric instrument (TGA, Netzsch STA449F31, Germany) with 10 °C min^{-1} from 20 to 800 °C under air atmosphere. The morphology analysis was demonstrated by high resolution transmission electron microscopy (HRTEM, FEI Tecnai G^2 TF30 S-Twin, Netherlands) and field emission scanning electron microscopy (FESEM, FEI Nova Nano SEM 450, USA). Meanwhile, FESEM was equipped with an energy-dispersive X-ray (EDX) analyzer from EDAX, Inc. After degassed at 300 °C for 6 h, N_2 adsorption–desorption isotherms were measured at −196 °C with an instrument of Micromeritics ASAP 2460 (USA). Additionally, the specific surface area of obtained ZSM-5 zeolite was calculated from the Brunauer–Emmett–Teller (BET) method, while the mesoporous volume and diameter were estimated by the Barrett–Joyner–Halenda (BJH) method, whilst the microporous volume and diameter were determined by the *t*-plot and Horvath–Kawazoe (H–K) methods, respectively. Finally, the particle size distributions were measured with the DLS method at 25 °C by NanoBrook Omni (Brookhaven, USA).

3 Results and discussion

3.1 Raw materials analysis

In our previous study,[30] the chemical properties and structure form of SiO_2 in A-1 were revealed in detail. Although A-1 consists of large amounts of amorphous nanometric silica, the presence of silanediol groups [$(OH)_2Si(OSi)_2$] seems like a negative aspect. It is indicated that ZSM-5 zeolite's formation is a dissolution-crystallization process, in which ill-ordered amorphous Si/Al sources would be turned into well-organized crystals.[26,31] Nevertheless, Kordatos *et al.*[28] demonstrated that the Si–OH groups could reduce the reactivity of silica during the synthesis process due to the destruction of SiO_4 in the silica framework. Fortunately, Al ingredients were also amorphous form in A-1 with a considerable amount, which made it as a natural Al source. In contrast, A-2 was rich in silica which was also amorphous nanoparticles with typical Si–O/Al–O structures, as shown in Fig. S1a and b,† whereas the chemical shift of −110 ppm in ^{29}Si MAS NMR (Fig. S1c†) meant that it was composed of Si–O tetrahedra [$Si(OSi)_4$], which was well suitable for synthesis of zeolite. As a consequence, SiO_4 sol was accelerated to nucleate and crystallize, while the short-range ion transport and nanometric size (Fig. S1d†) facilitated to the substitution of partial Si atoms with Al atoms to form AlO_4 in the process of ZSM-5 zeolite synthesis.

3.2 ZSM-5 zeolite characterization

The hydrothermal synthesis of aluminosilicate sol–gel to prepare ZSM-5 zeolite was carried out at the temperature range from 120 to 210 °C with the time horizon from 3 to 72 h, and the results for each specific scheme were shown in Table S2.† Thereafter, XRD results (Fig. S2†) demonstrated that the optimal conditions were 120 °C/48 h, 150 °C/36 h, 180 °C/24 h, and 210 °C/6 h, labelled with Z-1, Z-2, Z-3, and Z-4, respectively (Table S3†). According to all the samples of crystalline phases (Fig. 1a), XRD diffraction peaks at 7.97°, 8.82°, 9.12°, 14.93°, 23.32° and 23.95°, which are attributed to the lattice planes of [101], [200], [111], [031], [051], [303] and [133] with *d*-spacing values of 1.11, 1.00, 0.97, 0.59, 0.38, 0.37 and 0.36 nm, respectively.[29,32] On account of the high SiO_2/Al_2O_3 ratio in samples, the diffraction peaks at 7.97° and 8.82° are particularly distinct when it comes to being compared with other peaks.[25] As illustrated in Fig. 1b, FTIR shoulder bands at 1230, 1090, 800, 550, and 450 cm^{-1} are associated with the chemical structures of ZSM-5 zeolite.[33] Herein, the bands at 1230 and 450 cm^{-1} are assigned to the external T–O (T = Si/Al) asymmetrical stretching and bending vibrations, respectively. Furthermore, the bands at 1090 and 800 cm^{-1} are attributed to internal Si–O–T asymmetrical and symmetrical stretching vibrations, respectively. The typical mode of double five-membered rings (D5MR) in ZSM-5 zeolite shows at 550 cm^{-1}. In addition, the peaks at 3680, 3440, and 1635 cm^{-1} belong to the stretching and bending vibrations of –OH in silanol groups or zeolitic water, respectively. From the viewpoint of the zeolite growth (Fig. 1f), colloidal sol treatment decreases the reaction time effectively, along with a well-organized crystal. With the temperature increasing, T–O units get sequential with the rearrangement and substitution of Si and Al species observed from the band at 1090 cm^{-1} narrowing down from sample Z-1 to Z-4.[34]

To make it clear that what structural forms of the Si or Al species are presented in ZSM-5 zeolites, ^{29}Si and ^{27}Al MAS NMR spectra are carried out, as shown in Fig. 1c and d. ^{29}Si MAS NMR spectra demonstrated that [$(AlO)_1Si(SiO)_3$] (−106 ppm) and [$Si(SiO)_4$] (−112 ppm) were the dominating forms companied with thimbleful [$(OH)_2Si(SiO)_2$] (−94 ppm) due to the presence of silanediol groups in the raw material of A-1. Moreover, the high SiO_2/Al_2O_3 molar ratio of zeolite samples results in a weak peak at −106 ppm. Concerning about ^{27}Al MAS NMR, it was found that the resonance peak at 53 ppm was associated with tetrahedral aluminum (AlO_4), whereas there was not octahedral aluminum (0 ppm), indicating that all the Al atoms were incorporated in ZSM-5 zeolite framework without remaining in the precursor colloidal solution,[35,36] which was in better agreement with the results of ^{29}Si MAS NMR. Substantially, thermal stability of ZSM-5 zeolite is excellent, while the samples were a mass loss for evaporation of absorbed water (∼100 °C) and

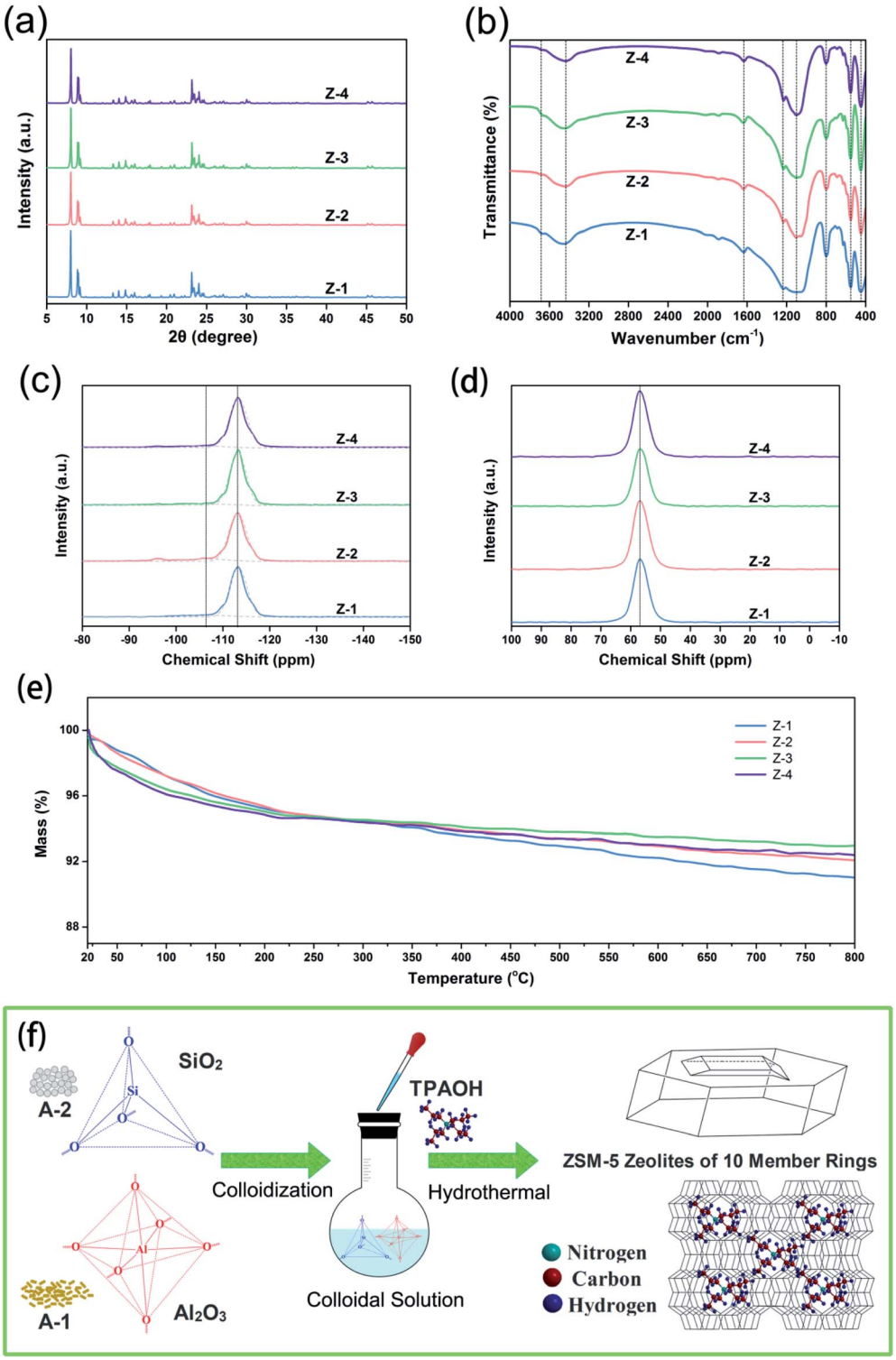

Fig. 1 XRD (a) and FTIR (b) profiles of synthesized ZSM-5 zeolites, ^{29}Si (c)/^{27}Al (d) MAS NMR, TGA (e) profiles of synthesized ZSM-5 zeolites, and hypothetical synthesis process (f) of ZSM-5 zeolites.

decomposition of little remaining TPA^+ (400–700 °C) as shown in Fig. 1e, but except for Z-1. In light of the poor rearrangement and substitution degree of AlO_4 in the Z-1 framework (Fig. 1b), the bond between the negative-charged zeolite structure and TPA^+ was not stronger.[37] Hence, the large amounts of residual free TPA^+ were more likely to prolong the decomposition time.

In some senses, crystal shapes could reflect the zeolite growth process indirectly.[38] As illustrated in Fig. 2a(1–4), the morphology variation was from cubical ellipsoid to coffin

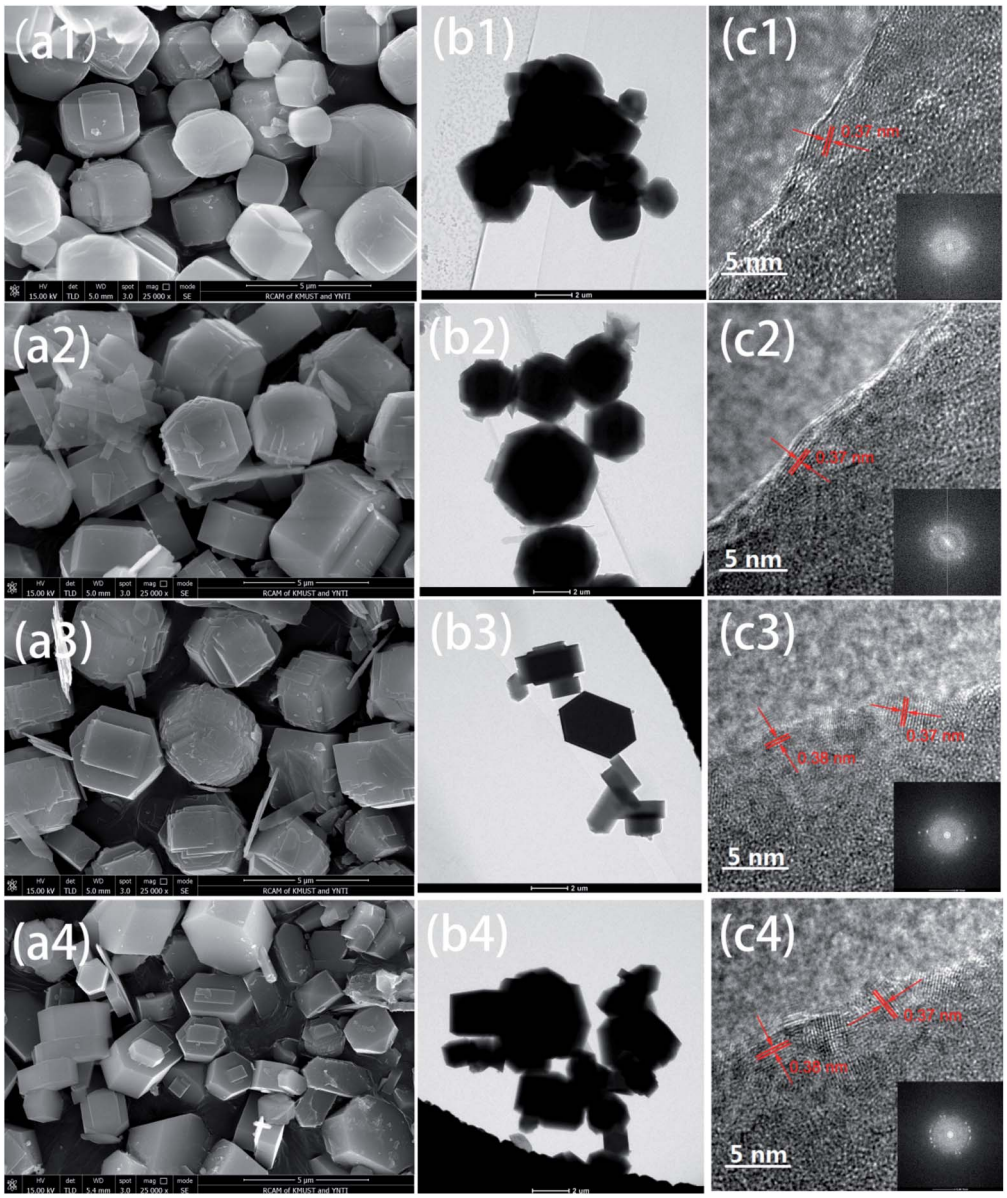

Fig. 2 Images of FESEM (a), TEM (b) and HRTEM (c) for lattice fringes with inset of SAED pattern: Z-1 (1), Z-2 (2), Z-3 (3) and Z-4 (4).

shape, which indicated that crystal pattern transition was occurring all the time observed from shape changes (Fig. S3†), whilst the reaction temperature played a more significant role in the evolution of crystal pattern and shape than reaction time on the whole. As seen from Fig. 2b, the synthesized ZSM-5 zeolite particles were thick in terms of the dark black background. Meanwhile, the electron beam was not able to penetrate the zeolite particles, whereas raising the voltage would destruct the zeolite framework solely, so the crystal lattice fringes could not be exhibited well.[35,36] Just like that, Fig. 2c illustrated that the lattice spacings from HRTEM images *via* Fast Fourier Transform (FFT) algorithm were 0.37 and 0.38 nm which were by the lattice planes of [303] and [051] in the XRD analysis. Additionally, the symmetrical diffraction spots around the central point in the SAED pattern demonstrated that ZSM-5 zeolite samples were crystal materials owning to the high crystallinity.[39]

On basis of the IUPAC classification,[40] the N_2 adsorption–desorption isotherm of ZSM-5 zeolites corresponds to type I isotherm due to microporous structure (Fig. 3a). In fact, the presence of hysteresis loops at high (P/P_0 = 0.5–0.9) and low pressures (P/P_0 = 0.15–0.4) is a universal phenomenon that emerged in many studies.[41–44] It has been proved that high-pressure hysteresis results from the aggregation of zeolite particles to form secondary mesoporous combined with microporous.[45] As for low-pressure hysteresis loops, it is a phenomenon that always happens to the synthesis of high siliceous ZSM-5 zeolites (Si : Al > 80).[46] Normally, intracrystalline microporous, an important part of crystal structure, with a channel size of MFI framework was 0.51 × 0.55 nm viewing

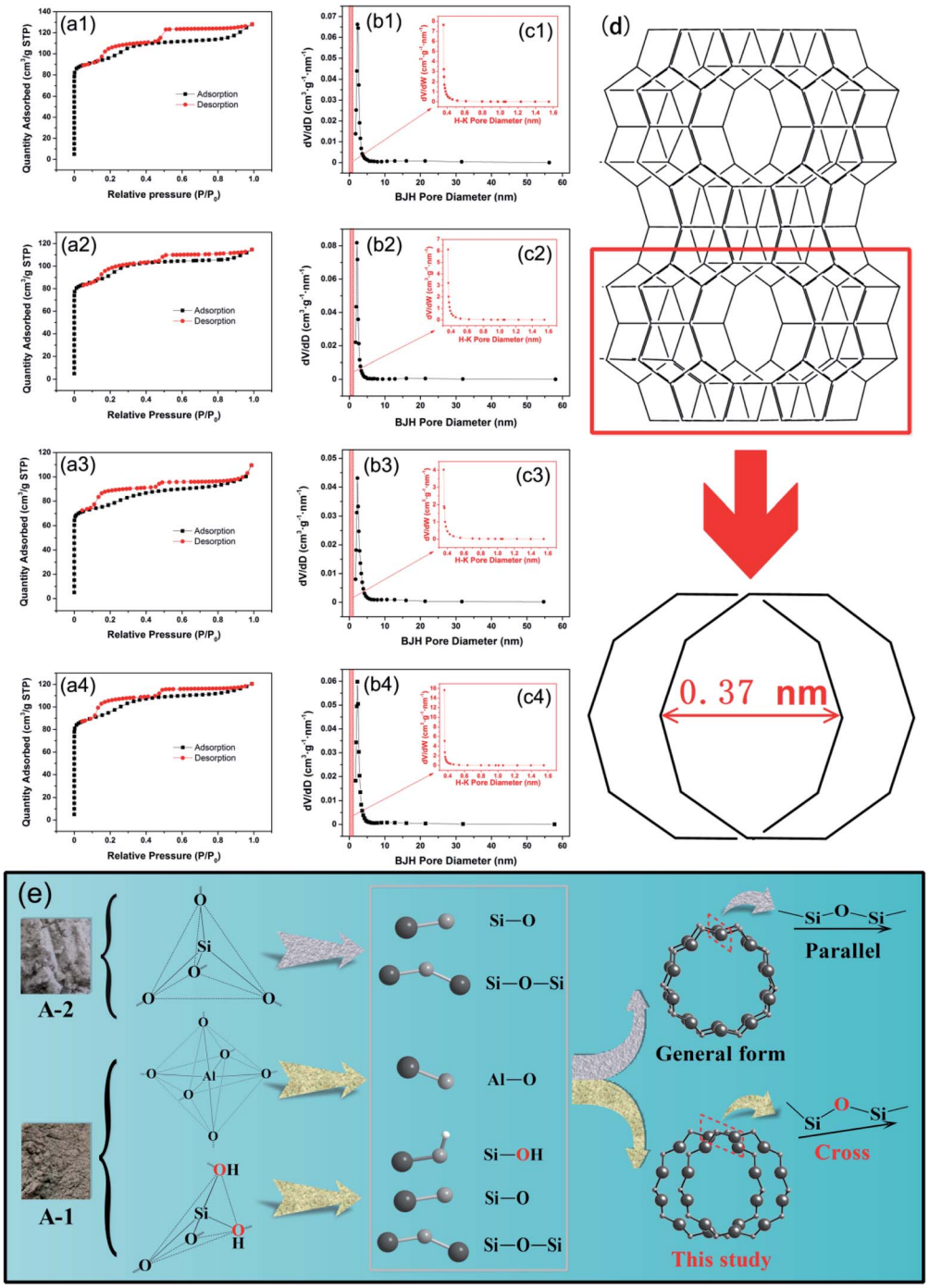

Fig. 3 N_2 adsorption–desorption isotherms (a), pore size distribution of mesoporous (b) and microporous (c), and a diagram of crossed 10MR in ZSM-5 zeolite samples (d) with hypothetical formation mechanism (highlight the unique influence of $SiO_2(OH)_2$ tetrahedron) (e) Z-1 (1), Z-2 (2), Z-3 (3) and Z-4 (4).

along [100] or 0.53 × 0.56 nm viewing along [010].[47] However, the ten-membered rings (10MR) would be crossed and overlapped, which shorten the microporous size,[42] as depicted in Fig. 3c and d. Thus, the change of pore size and geometry could facilitate a phase transition of adsorbate to influence adsorbent–adsorbate interaction force, which results in hysteresis loops derived from the difference between adsorption and desorption rate at low pressure.[43,46,48]

In this study, the low pressure hysteresis loops occurred at $P/P_0 = 0.15$.[48] As aforementioned, the crossed 10MR made the microporous size narrowed and concentrated at 0.37 nm leading to distinct low-pressure hysteresis loops. The formation of crossed 10MR can be contributed to the presence of Si–OH in A-1, which might change the bond angle due to the superior force of the H atom during the rearrangement and generation of ZSM-5 zeolites. Therefore, Si–O–Si atoms that are in a horizontal

state normally were slant actually in this study, which resulted in the phenomenon of crossed 10MR (Fig. 3e). Then, Table S4† indicates that S_{BET} decreases firstly and increases later along with reaction temperature increasing with S_{BET} of 300 $m^2\ g^{-1}$ and V_{micro} of 0.08 $cm^3\ g^{-1}$ on average, whereas S_{micro} is just the opposite which means that the intracrystalline microporous may collapse at higher reaction temperature (>180 °C). Herein, the pore volume of Z-3 is the largest in all the samples, whatever microporous or mesoporous volumes. Furthermore, Z-3 has a relative small particle size coupled with a relative large pore size. Despite the smallest S_{BET} of Z-3, the microporous properties and porosity are of great concern with regard to zeolite adsorbent, while Z-3 has optimal microporous properties, which is the best choice for dye adsorbent.

3.3 Adsorption performance evaluation

The utilization of zeolite adsorbents to remove dyes from aqueous has been proved to be feasible.[49–51] In this study, the dye adsorbing effectiveness of ZSM-5 zeolite was novel to be contraposed at cationic (MB) and anionic (CR) dyes for investigation on the variation of adsorption quantity under diverse conditions. When the concentration of dye aqueous was 25 mg L^{-1}, the removal efficiency of MB was more than 90%, whereas that of CR was less than 80% (Table S5†), and it was essential that there are different interaction forces between adsorbates and adsorbents, particularly to pay attention to the influence of positive and negative charges in the dye adsorption process. As illustrated in Fig. S5,† it is found that MB and CR dyes are adsorbed uniformly and steady surrounding the zeolites whose surfaces are coated with dyes to be smooth in SEM images, and the adsorbing MB amount of zeolite is larger than CR. From the EDX analysis, it is estimated that the SiO_2/Al_2O_3 molar ratio of ZSM-5 zeolite is approximately 400, which indicated that more silicon sources were dissolved in mother liquid compared with aluminum sources. Afterwards, it was evident that the $q_{e,exp}$ of MB was increasing coupled with temperature increasing, whereas that of CR was inverse, and the maximum adsorption quantity of MB was larger than that of CR simultaneously, as depicted in Fig. S6 and S7.† Generally speaking, two interaction forces are involved in adsorption process:[52] One is the attraction of adsorbate–adsorbent; the other is the repulsion between adsorbate molecules. To clarify the adsorption equilibrium and interaction relationship between dye molecules (adsorbate) and ZSM-5 zeolite (adsorbent), it is essential to construct isothermal models in terms of assumed conditions (eqn (4)–(9) shown in ESI†), *e.g.* Langmuir, Freundlich, Temkin, Sips, Redlich–Peterson, *etc.*

Referring to the Giles' classification,[53] the experimental equilibrium isotherm plots illustrated in Fig. 4 demonstrates that the adsorption isotherms of MB and CR using synthesized zeolite are both in accordance with Ostwald and de Izaguirre (L2-type) curve, which indicates that the dye molecules are adsorbed flat on the zeolite surface. From the view of isotherm models (Table S5a†), the q_{max} of MB (120–160 mg g^{-1}) was larger than that of CR (36–87 mg g^{-1}), probably due to the difference electrostatic interaction between dye molecules and negative charge AlO_4 of zeolite framework. Among all the five models, the isotherm equilibrium curve of MB was well assigned to the Redlich–Peterson model, and that of CR was attributed to the Sips model in terms of correlation coefficient (R^2). Simultaneously, referring to the R^2 result of the Langmuir model, adsorption of MB was more homogeneous than that of CR, while the γ value of MB is closer to 1 than that of CR which means that the MB was adsorbed on the zeolite surface more uniformly than CR. Furthermore, the adsorption processes of MB and CR *via* ZSM-5 zeolite were favourable from the evaluation of the values of R_L and $1/n$. Additionally, it was shown that the values of K_T and b_T of adsorbing MB were smaller than those of adsorbing CR which demonstrated that the interaction forces between CR molecules and zeolite were stronger, and the

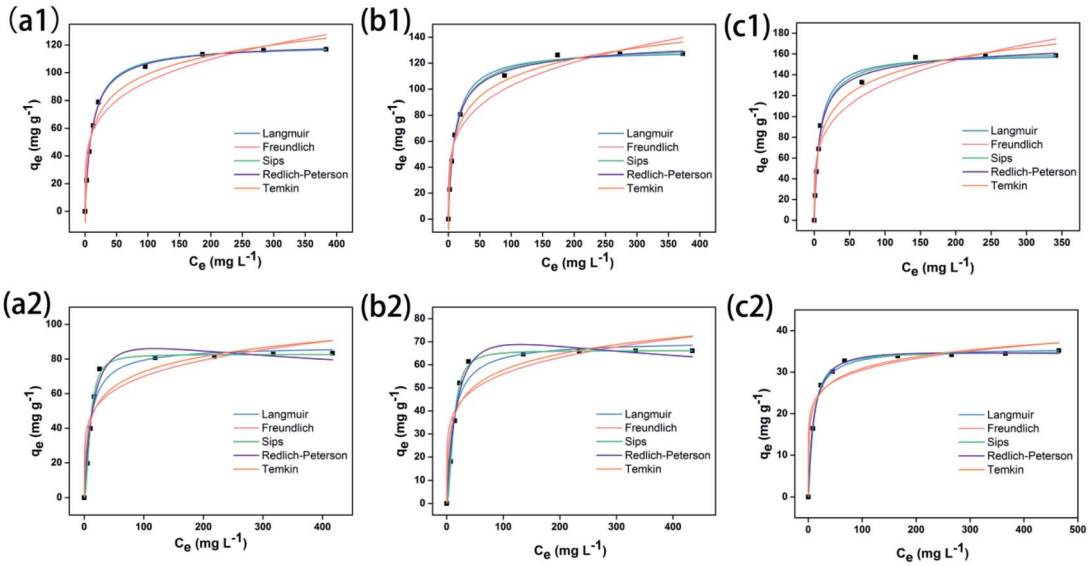

Fig. 4 Experimental and isothermal modelled equilibrium plots for MB (1) and CR (2): 25 °C (a), 45 °C (b) and 65 °C (c).

adsorbing rate was more rapider at the initial time when it came to comparing with MB in accordance with Fig. 4. In brief, utilization of ZSM-5 zeolite to adsorb MB and CR is facile, and the adsorption of MB can be regarded as a homogeneous adhesion process, whereas the adsorption of CR is a heterogeneous system with intense interaction forces.

Substantially, the diffusion of dyes in the solution can be divided into four consecutive stages.[54] Firstly, the dye molecules diffuse in the liquid phase. Secondly, molecules diffuse across the liquid film surrounding the adsorbent surface. Thirdly, molecules diffuse into the adsorbent particle inside. Lastly, physisorption or chemisorption takes place on the adsorption active sites. Thereof, pseudo-first-order (PFO), pseudo-second-order (PSO), and intraparticle diffusion kinetic models are used to describe adsorption kinetic mechanisms in line with the diffusion steps (eqn (10)–(12) shown in ESI†). Owing to all the values of R^2 in the PSO model verging to 0.99 on average (Table S5b†) compared with the R^2 values close to 0.92–0.99 in the PFO model, it is demonstrated that utilization of ZSM-5 zeolite adsorbent to adsorb dye molecules is adequately associated with the PSO model, whatever adsorbing MB or CR dye. Coincident results can also be seen from Fig. 5a and b. In addition, the calculated equilibrium adsorption quantity ($q_{e,cal}$) from the PSO model is in better agreement with $q_{e,exp}$ than that from the PFO model. As far as the intraparticle diffusion model is concerned (Fig. 5c), all the values of C_i are non-null, which means that there are other diffusional phenomena to control the adsorption rate, not only the intraparticle diffusion. In the intraparticle diffusion process, the initial diffusion rate of MB is faster than that of CR, contrarily to the initial rate of the whole adsorption process aforementioned. It is revealed that the adsorption of MB underwent three stages: (1) external surface adsorbing, (2) porous channel diffusion, and (3) internal surface adsorbing. However, the latter step was absent in the adsorbing CR process, which may result from the larger molecular weight of CR.

To evaluate the thermodynamic properties during the zeolite adsorption process of MB and CR dyes, the parameters of ΔG^0, ΔH^0, ΔS^0, and E_a were put forward (eqn (13)–(17) shown in ESI†) coupled with van't Hoff and Arrhenius plots in Fig. S8.† On the one hand, both the values of ΔH^0 and ΔS^0 are positive during the adsorption of MB dye (Table S5c†), which confirms that this is an endothermic process along with confusion degree increasing, and it is verified that the interaction force between zeolite and MB dye is strong. Contrarily, the values of ΔH^0 and ΔS^0 for adsorbing CR dye are negative, which means that it is an exothermic process with confusion degree decreasing. On the other hand, the values of ΔG^0 are negative which indicates that either MB or CR adsorption process is spontaneous and favorable. Meanwhile, the values of ΔG^0 are in the range from −20 to 0 kJ mol^{-1},[55] and the values of E_a are in the range from 5 to 40 kJ mol^{-1},[56] which proves that the adsorption processes of MB and CR dyes with zeolites are both physisorptions. It can be anticipated that the dye molecules adsorbing onto ZSM-5 zeolite surface may result from van der Waals forces at low temperature, but the influence on electrostatic interaction cannot be ignored at high temperature. For example, the negative charge framework of zeolite will increase the adsorption quantities of cationic dye (MB) by attracting, and decrease the adsorption quantities of anionic dye (CR) by repulsion, as shown in Fig. 6a.

Based upon the thermodynamic analysis of contaminated zeolites (Fig. 6b), a distinct mass loss was happened at around 550 °C, which is assigned to the decomposition of MB and CR dyes in the zeolites. Hence, the regeneration temperature of contaminated zeolites was determined at 550 °C for 2 h. In this case, the $q_{e,exp}$ was decreased from 158.52 to 116.51 mg g^{-1} after 5 cycles of regeneration utilization ($q_{e5,exp}$) for adsorbed MB, compared with the variation from 83.36 to 63.62 mg g^{-1} of CR, as illustrated in Fig. 6c and d. On the whole, the AE of regeneration zeolite for MB was stabilization in 70%, contrarily to CR in 75% approximately, which demonstrates that the ZSM-5

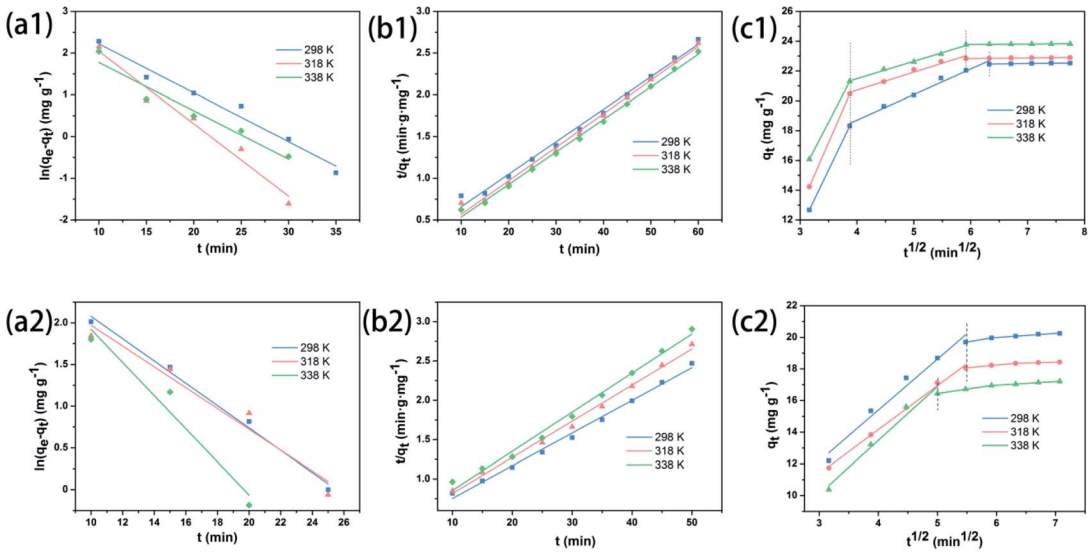

Fig. 5 Experimental and kinetic modelled linear plots for MB (1) and CR (2) at 25 mg L^{-1} initial dye concentration: pseudo-first order (a), pseudo-second order (b) and intraparticle diffusion (c) models.

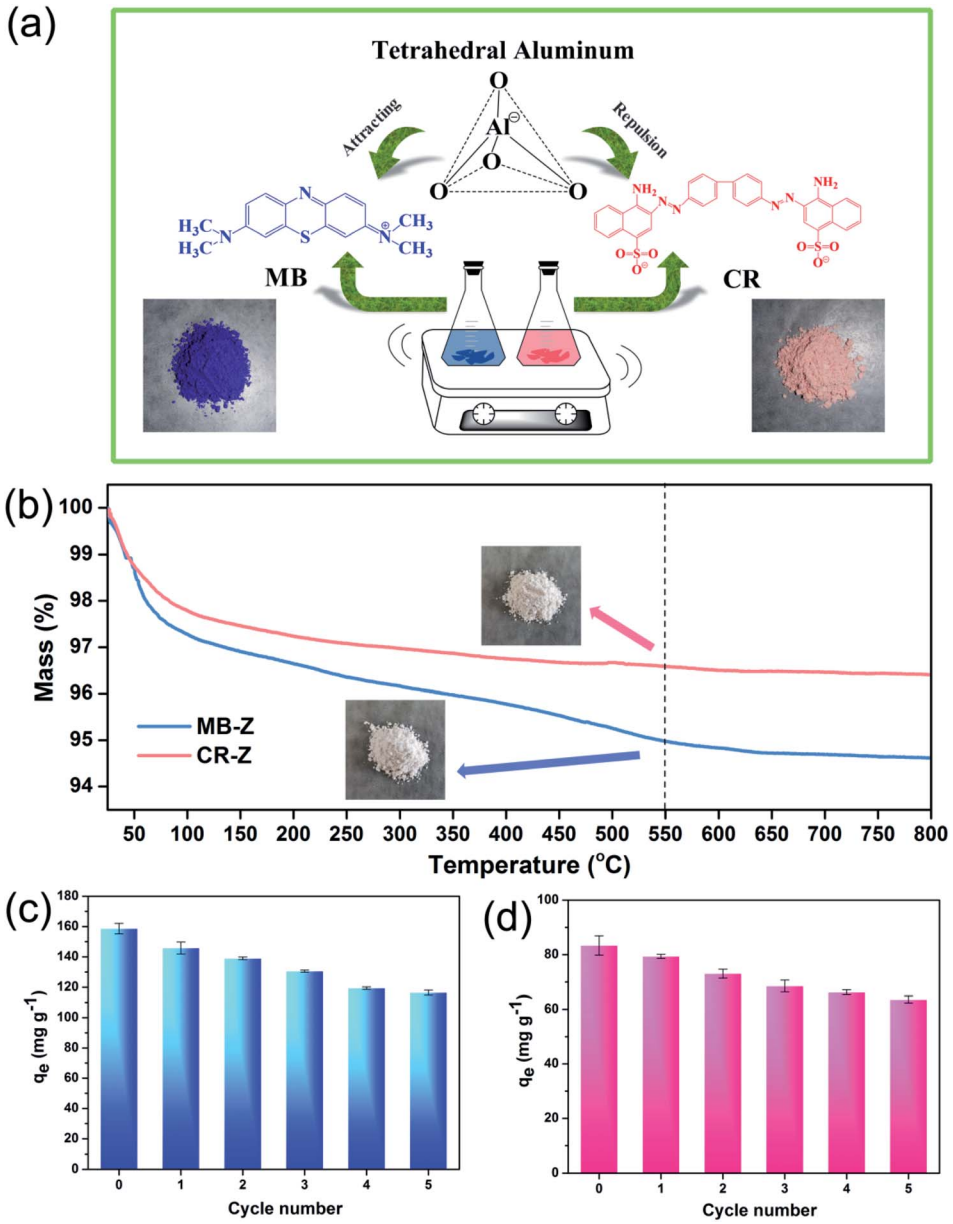

Fig. 6 Hypothetical adsorption process (a) of electrostatic interaction between zeolites and dyes. TGA profiles (b) of contaminated ZSM-5 zeolites. The variation of maximum adsorption quantities for MB (c) and CR (d) dyes with regeneration zeolites.

zeolite samples are suitable for regeneration and reusability for reutilization.

4 Conclusions

ZSM-5 zeolites are successfully synthesized from biomass power plant ash blending of complementary rice husk ash by colloidal sol hydrothermal method. It is found that the sample zeolites have the typical Si–O and Al–O structures with a micrometer shape of the coffin at temperatures of 120, 150, 180, and 210 °C for times of 48, 36, 24, and 6 h, respectively. Interestingly, the 10MR of ash ZSM-5 zeolites are crossed and overlapped, which enriches the porosity of zeolite adsorbent. Under these conditions, the BET surface area is in the range of 250 to 320 $m^2\ g^{-1}$, while the microporous volume varies from 0.07 to 0.10 $cm^3\ g^{-1}$. Subsequently, the adsorption process of MB and CR is a spontaneous and favourable physisorption associated with electrostatic interaction. Otherwise, the adsorption isotherm of adsorbing MB is conforming to the Redlich–Peterson model tendency to homogeneity accompanied with an endothermic process and confusion degree increasing, whereas the Sips model is suitable for adsorption of CR in a heterogeneous system, which is exothermic and confusion degree decreasing. To clarify the value of synthesized zeolites for reusable removal of dyes, the regeneration and recycle tests are carried out, which indicates that the adsorption efficiency for either MB or CR dye can be stabilization in more than 70%, and lives up to the target of waste controlled by waste. From a long-term perspective, it is

feasible that ash zeolites can be sustainable to remove the dyes from textile effluents.

Conflicts of interest

The authors declare that they have no known competing financial interests or personal relationships that could have appeared to influence the work reported in this paper.

Acknowledgements

The authors thank the financial supports provided by the National Natural Science Foundation of China (Grant 21766013).

References

1 J. He, R. Zhu and B. Lin, *J. Cleaner Prod.*, 2019, **237**, 117783.
2 Q. Tan, T. Wang, Y. Zhang, X. Miao and J. Zhu, *Energy*, 2017, **139**, 1066–1079.
3 J. Liu, S. Wang, Q. Wei and S. Yan, *Energy Policy*, 2014, **70**, 144–151.
4 G. M. Joselin Herbert and A. Unni Krishnan, *Renewable Sustainable Energy Rev.*, 2016, **59**, 292–308.
5 B. Lin and J. He, *Renewable Sustainable Energy Rev.*, 2017, **73**, 1218–1230.
6 X. Zhao, Q. Cai, S. Li and C. Ma, *Renewable Sustainable Energy Rev.*, 2018, **95**, 242–253.
7 S. V. Vassilev, D. Baxter, L. K. Andersen and C. G. Vassileva, *Fuel*, 2013, **105**, 40–76.
8 S. V. Vassilev, D. Baxter and C. G. Vassileva, *Fuel*, 2013, **112**, 391–449.
9 N. C. Cruz, F. C. Silva, L. A. C. Tarelho and S. M. Rodrigues, *Resour., Conserv. Recycl.*, 2019, **150**, 104427.
10 G. Liang, Y. Li, C. Yang, C. Zi, Y. Zhang, D. Zhang, M. Wang and W. Zhao, *Energy Sources, Part A*, 2020, 1–12.
11 F. Piri, A. Mollahosseini, A. Khadir and M. M. Hosseini, *J. Environ. Chem. Eng.*, 2019, **7**, 103338.
12 G. V. Brião, S. L. Jahn, E. L. Foletto and G. L. Dotto, *J. Colloid Interface Sci.*, 2017, **508**, 313–322.
13 P. V. Nidheesh, M. Zhou and M. A. Oturan, *Chemosphere*, 2018, **197**, 210–227.
14 E. Alventosa-deLara, S. Barredo-Damas, M. I. Alcaina-Miranda and M. I. Iborra-Clar, *J. Hazard. Mater.*, 2012, **209–210**, 492–500.
15 D. E. Kritikos, N. P. Xekoukoulotakis, E. Psillakis and D. Mantzavinos, *Water Res.*, 2007, **41**, 2236–2246.
16 G. Muthuraman, *Desalination*, 2011, **277**, 308–312.
17 S. M. d. A. G. U. de Souza, K. A. S. Bonilla and A. A. U. de Souza, *J. Hazard. Mater.*, 2010, **179**, 35–42.
18 R. Nodehi, H. Shayesteh and A. R. Kelishami, *Microchem. J.*, 2020, **153**, 104281.
19 S. V. Vassilev, D. Baxter, L. K. Andersen and C. G. Vassileva, *Fuel*, 2013, **105**, 19–39.
20 M. Shaban, M. R. Abukhadra, M. G. Shahien and S. S. Ibrahim, *Environ. Chem. Lett.*, 2018, **16**, 275–280.
21 S. Oukil, F. Bali and D. Halliche, *Sep. Sci. Technol.*, 2019, 1–17.
22 R. Sabarish and G. Unnikrishnan, *Carbohydr. Polym.*, 2018, **199**, 129–140.
23 R. N. M. Missengue, P. Losch, G. Sedres, N. M. Musyoka, O. O. Fatoba, B. Louis, P. Pale and L. F. Petrik, *C. R. Chim.*, 2017, **20**, 78–86.
24 H. Li, R. Cheng, Z. Liu and C. Du, *Sci. Total Environ.*, 2019, **683**, 638–647.
25 S. Han, Y. Liu, C. Yin and N. Jiang, *Microporous Mesoporous Mater.*, 2019, **275**, 223–228.
26 Y. Yue, Y. Kang, Y. Bai, L. Gu, H. Liu, J. Bao, T. Wang, P. Yuan, H. Zhu, Z. Bai and X. Bao, *Appl. Clay Sci.*, 2018, **158**, 177–185.
27 M. K. Naskar, D. Kundu and M. Chatterjee, *J. Am. Ceram. Soc.*, 2012, **95**, 925–930.
28 K. Kordatos, A. Ntziouni, L. Iliadis and V. Kasselouri-Rigopoulou, *J. Mater. Cycles Waste Manage.*, 2013, **15**, 571–580.
29 K. Kordatos, S. Gavela, A. Ntziouni, K. N. Pistiolas, A. Kyritsi and V. Kasselouri-Rigopoulou, *Microporous Mesoporous Mater.*, 2008, **115**, 189–196.
30 G. Liang, Y. Li, C. Yang, C. Zi, Y. Zhang, X. Hu and W. Zhao, *Waste Manage.*, 2020, **105**, 8–17.
31 H. Hamdan, M. N. M. Muhid, S. Endud, E. Listiorini and Z. Ramli, *J. Non-Cryst. Solids*, 1997, **211**, 126–131.
32 K. P. Dey, S. Ghosh and M. K. Naskar, *Ceram. Int.*, 2013, **39**, 2153–2157.
33 Y. Li, G. Liang, L. Chang, C. Zi, Y. Zhang, Z. Peng and W. Zhao, *Energy Sources, Part A*, 2021, **43**, 1745–1758.
34 W. Luo, X. Yang, Z. Wang, W. Huang, J. Chen, W. Jiang, L. Wang, X. Cheng, Y. Deng and D. Zhao, *Microporous Mesoporous Mater.*, 2017, **243**, 112–118.
35 G. Song, D. Xue, J. Xue and F. Li, *Microporous Mesoporous Mater.*, 2017, **248**, 192–203.
36 M. Li, I. N. Oduro, Y. Zhou, Y. Huang and Y. Fang, *Microporous Mesoporous Mater.*, 2016, **221**, 108–116.
37 S. Narayanan, J. J. Vijaya, S. Sivasanker, L. J. Kennedy and S. K. Jesudoss, *Powder Technol.*, 2015, **274**, 338–348.
38 W. Panpa and S. Jinawath, *Appl. Catal., B*, 2009, **90**, 389–394.
39 C. Zhang, S. Li and S. Bao, *Res. Chem. Intermed.*, 2018, **44**, 3581–3595.
40 K. S. W. Sing, D. H. Everett, R. A. W. Haul, L. Moscou, R. A. Pierotti, J. Rouquerol and T. Siemieniewska, *Pure Appl. Chem.*, 1985, **57**, 603–619.
41 D. Hartanto, R. Kurniawati, A. B. Pambudi, W. P. Utomo, W. L. Leaw and H. Nur, *Solid State Sci.*, 2019, **87**, 150–154.
42 Y.-J. Wang, J.-P. Cao, X.-Y. Ren, X.-B. Feng, X.-Y. Zhao, Y. Huang and X.-Y. Wei, *Fuel*, 2020, **268**, 117286.
43 E. Panayi and C. Theocharis, *Stud. Surf. Sci. Catal.*, 2007, **160**, 273–278.
44 Y. Tian, B. Zhang, H. Liang, X. Hou, L. Wang, X. Zhang and G. Liu, *Appl. Catal., A*, 2019, **572**, 24–33.
45 C. Zhang, S. Li and S. Bao, *Waste Biomass Valorization*, 2019, **10**, 2825–2835.
46 S. Kaskel, P. Llewellyn, F. Rodriguez-Reinoso and N. A. Seaton, *Characterisation of Porous Solids VIII:*

Proceedings of the 8th International Symposium on the Characterisation of Porous Solids, The Royal Society of Chemistry, 2009, pp. 182–189.

47 Y. Wang, T. Du, X. Fang, H. Jia, Z. Qiu and Y. Song, *Mater. Chem. Phys.*, 2019, **232**, 284–293.

48 G. Kyriakou and C. R. Theocharis, *The Anomalous Sorptive Behaviour Of ZSM-5 And Silicalite-I: Observation Of Low-Pressure Hysteresis In Nitrogen Adsorption*, Elsevier, 2002, vol. 144, pp. 709–716.

49 A. K. Hammed, N. Dewayanto, D. Du, M. H. Ab Rahim and M. R. Nordin, *J. Environ. Chem. Eng.*, 2016, **4**, 2607–2616.

50 S. K. Hassaninejad-Darzi, S. Kavyani, M. Torkamanzadeh and R. Dianati Tilaki, *Monatsh. Chem.*, 2017, **148**, 2037–2049.

51 Y. Zhang, F. Jin, Z. Shen, F. Wang, R. Lynch and A. Al-Tabbaa, *Chemosphere*, 2019, **220**, 422–431.

52 G. I. Supelano, J. A. Gómez Cuaspud, L. C. Moreno-Aldana, C. Ortiz, C. A. Trujillo, C. A. Palacio, C. A. Parra Vargas and J. A. Mejía Gómez, *Fuel*, 2020, **263**, 116800.

53 C. H. Giles, T. H. McEwan, S. N. Nakhawa and D. Smith, *J. Chem. Soc.*, 1960, 3973–3993.

54 K. V. Kumar, V. Ramamurthi and S. Sivanesan, *J. Colloid Interface Sci.*, 2005, **284**, 14–21.

55 Y. Yu, Y.-Y. Zhuang and Z.-H. Wang, *J. Colloid Interface Sci.*, 2001, **242**, 288–293.

56 H. Nollet, M. Roels, P. Lutgen, P. Van der Meeren and W. Verstraete, *Chemosphere*, 2003, **53**, 655–665.